

A ROTOR TRANSITION PREDICTION METHOD BASED ON GALILEAN INVARIANCE AND THE C1 CROSSFLOW TRANSITION CRITERION

Zhou Kangyuan[1,2], Song Wenping[1,2], Xu Jianhua[1,2,*]

[1]School of Aeronautics, Northwestern Polytechnical University, Xi'an 710071, P. R. China
[2]National Key Laboratory of Aircraft Configuration Design, Xi'an 710072, P. R. China

Abstract

The rotor is the core aerodynamic component of a helicopter, and its aerodynamic performance directly determines the helicopter's speed, load capacity, maneuverability, and mission capability. Accurate prediction of rotor boundary layer transition characteristics is fundamental to refined aerodynamic analysis and laminar flow drag reduction design. Among existing transition prediction methods, the $\gamma-\widetilde{\mathrm{Re}}_{\theta t}$ transition model offers significant advantages in engineering applications due to its robustness and efficiency. However, this model cannot account for crossflow transition effects and does not satisfy Galilean invariance under rotating coordinate systems, which limits its application to transition prediction for complex rotor flows. To address these shortcomings, this paper develops a transition prediction method suitable for three-dimensional rotor flows: the $G-\gamma-\widetilde{\mathrm{Re}}_{\theta t}-C1$ transition prediction model. This model replaces the velocity-related terms in the original model with Galilean invariants such as strain rate and vorticity, thereby eliminating the dependence on the coordinate system, and incorporates the C1 crossflow transition criterion to enable identification of crossflow transition. The developed transition prediction model is coupled with an unsteady RANS solver to establish a high-fidelity unsteady RANS solver (PMNS3DR-T) that can automatically predict rotor transition. Comparison with PSP rotor transition experimental results shows that the proposed transition prediction model and the PMNS3DR-T solver can accurately predict the transition location and aerodynamic performance of the rotor, providing a reliable high-fidelity analysis tool for refined aerodynamic simulation and laminar flow design of rotors.

Keywords: Helicopter rotor, Galilean invariance, $G-\gamma-\widetilde{\mathrm{Re}}_{\theta t}-C1$ transition prediction model, PMNS3DR-T

1. Introduction

Boundary-layer transition is one of the core issues in fluid mechanics, with research aimed at accurately modeling the physical process of flow evolution from laminar to turbulent states and revealing its dominant mechanisms. The transition location directly determines the skin friction drag on the surface of an aircraft and the ability to resist separation of the boundary layer, thereby significantly affecting its aerodynamic performance and handling qualities. Therefore, achieving accurate prediction of boundary-layer transition is an essential foundation for the refined aerodynamic design and high-fidelity performance evaluation of aircraft.

The importance and challenge of transition research become even more pronounced when focusing on helicopter rotors as a special case. Wind tunnel experiments[1][2] have shown that, whether in hover or forward flight, distinct laminar flow regions exist on the rotor surface, exhibiting a certain ability to maintain laminar flow. Conducting research on rotor boundary-layer transition helps improve the accuracy of aerodynamic performance evaluation, explore the transition evolution mechanisms under complex flow environments, and provide support for engineering-oriented laminar drag reduction design and assessment. The AIAA Rotor Hover Prediction Workshop[3] also identifies boundary-layer transition prediction methods as one of the key scientific and technological issues for enhancing the predictive accuracy of rotor hover performance.

However, rotor blades operate in an extreme environment characterized by high-speed rotation coupled with intense unsteady inflow. The flow simultaneously involves three-dimensional rotational effects, severe dynamic stall, and strong unsteady features, leading to significant differences in boundary-layer development and instability mechanisms compared with fixed wings. Most classical transition models are established based on two-dimensional or quasi-three-dimensional, steady or weakly unsteady flows. The Tollmien–Schlichting wave instability on which they focus may not be the dominant mechanism in rotor flow fields. Instead, crossflow instability

induced by three-dimensional pressure gradients, rotational effects, and unsteady pressure variations is more likely to be the key factor.

To accurately predict rotor transition characteristics, many studies have compared the predictive accuracy and applicability of different transition models. For example, Sheng et al.[4] conducted numerical investigations on a full-scale XV-15 tiltrotor, systematically analyzing the effects of grid resolution and transition model on hover efficiency prediction. Their results showed that the laminar flow range predicted by the SST-based transition model was larger than that predicted by the SA model and agreed better with experimental data. Byung Young Min et al.[5] further compared the differences in transition prediction between the two models using the OVERFLOW software, explained the reasons from the perspective of intermittency factor distribution evolution, and pointed out that transition effects and variations in turbulence intensity have a non-negligible impact on the evaluation of rotor hover efficiency. Jared A. Carnes et al.[6] adopted the hybrid RANS/LES-coupled transition prediction method to perform refined evaluations of the aerodynamic characteristics of the HVAB rotor. In comparison with the fully turbulent RANS results of Singh et al.[7], they found that the hover efficiency predicted by the hybrid method was higher than that of the fully turbulent results but still lower than the predictions obtained using a transition model. Fu Song's team at Tsinghua University[8] conducted numerical studies on the boundary-layer transition characteristics of the XV-15 rotor in hover using a self-developed three-equation k-ω-γ transition model. They pointed out that future work should further consider the effects of crossflow and turbulence enhancement induced by incoming vortical disturbances on transition prediction. In addition, Lee et al.[9] emphasized the importance of satisfying the Galilean invariance of transition models in rotor numerical simulations. Models that do not satisfy this property are prone to unphysical phenomena, such as abnormal transition location predictions[10] and non-physical high turbulence intensity distributions[11], and therefore necessary modifications to the velocity-related terms are required.

Current research indicates that although the $\gamma-\widetilde{\mathrm{Re}}_{\theta,t}$ transition model can predict, to some extent, the transition in regions with two-dimensional characteristics such as the midspan of a blade, it still exhibits obvious deficiencies in complex flow regions of a rotor blade due to its construction based on streamwise transition correlations under a stationary coordinate system. Therefore, further development is urgently needed. Specifically, two key issues remain insufficiently addressed: (1) The model does not satisfy the covariance requirement in a moving coordinate system. Key parameters in the existing model, such as the pressure gradient factor and turbulence intensity, depend on velocity quantities in the reference frame and thus lack Galilean invariance in a rotating coordinate system. This tends to produce unphysical transition predictions in rotor flow simulations, compromising the reliability and consistency of the predictions. (2) The influence of crossflow instability is not adequately considered. During rotor rotation, the Coriolis force induces significant spanwise flow, which readily triggers crossflow transition. However, current mainstream transition models are primarily constructed for transition mechanisms induced by streamwise Tollmien–Schlichting waves, and thus urgently need to be extended with crossflow transition prediction capabilities.

To address the above issues, this paper carries out the following research tasks. First, the velocity-related terms in the original $\gamma-\widetilde{\mathrm{Re}}_{\theta,t}$ model are replaced by Galilean invariants such as strain rate and vorticity to remedy the covariance deficiency of the original model. Second, the crossflow transition C1 criterion is introduced to extend the model's capability for predicting crossflow transition, leading to the development of the $G-\gamma-\widetilde{\mathrm{Re}}_{\theta,t}-C1$ model. Finally, the improved model is coupled with an unsteady RANS solver, and the predictive capabilities of the improved model and traditional models are compared and analyzed based on experimental transition data of the PSP rotor, thereby validating the effectiveness of the proposed method.

The structure of this paper is as follows. Section 1 is an introduction that elaborates on the necessity and difficulties of developing a rotor transition prediction method. Section 2 presents the developed transition prediction method. Section 3 compares the prediction accuracy of different methods based on the experimental transition data of the PSP rotor and validates the effectiveness of the proposed method. Section 4 provides a summary and outlines plans for future research.

2. Model Development and Numerical Implementation

To address the characteristics of rotor flows, this paper systematically improves the $\gamma-\widetilde{\mathrm{Re}}_{\theta,t}$ transition model. Galilean invariants are employed to replace and rewrite the velocity-related terms in the original model, remedying its covariance deficiency. On this basis, the crossflow transition C1 criterion is incorporated, enabling the model to effectively identify crossflow transition induced

by the Coriolis force in rotor flows. This section briefly introduces the developed $G-\gamma-\widetilde{\mathrm{Re}}_{\theta,t}-C1$ transition model and its coupling approach with the unsteady RANS solver.

2.1 Covariance Correction Based on Galilean Invariance

The original $\gamma-\widetilde{\mathrm{Re}}_{\theta,t}$ transition model was proposed by Menter and Langtry in 2006[12]. Its core idea is to relate the traditional boundary-layer integral parameter to local flow-field variables through empirical correlations, and to introduce a transport equation for the intermittency factor γ to describe the gradual process from laminar to turbulent flow. The entire model does not rely on the identification of the boundary-layer edge or normal integration, and thus exhibits good adaptability to complex geometries, unstructured grids, and large-scale parallel computations. However, the model implicitly depends on the reference frame. The definitions of several key parameters depend on the streamwise coordinate direction of the computational grid or on velocity values relative to the reference frame. As a result, when applied to engineering problems involving relative motion, such as rotors and turbomachinery, the model produces non-physical differences in transition predictions under different computational reference frames, thereby limiting its generality and predictive consistency. Specifically, the aspects that violate covariance are as follows:

(1) The pressure gradient parameter λ_θ depends on the streamwise coordinate: The pressure gradient parameter $\lambda_\theta=\frac{\rho\theta^2}{\mu}\frac{d|\vec{u}|}{ds}$ in the transition model relies on the velocity gradient $\frac{d|\vec{u}|}{ds}$ and does not satisfy covariance under reference frame transformation.

(2) The definition of turbulence intensity depends on the reference frame: In the empirical correlation for the critical momentum thickness Reynolds number $\mathrm{Re}_{\theta c}$, the turbulence intensity is expressed as $Tu=\sqrt{\frac{2}{3}k}\frac{1}{|\vec{u}|}$, where $|\vec{u}|$ is the magnitude of the local velocity. Under Galilean transformation ($x'=x-vt$), $|\vec{u}|$ changes, causing both the turbulence intensity and the associated transition criterion to depend on the choice of reference frame.

(3) The transport equation for the momentum thickness Reynolds number depends on the coordinate system: Both the convection term and the source term in the transport equation of $\widetilde{\mathrm{Re}}_{\theta,t}$ contain velocity components, and the construction of the source term involves streamwise derivative operations, which depend on the selection of the reference frame.

To achieve covariance correction, all reference-frame-dependent quantities must be replaced by Galilean invariants. In fluid mechanics, quantities that satisfy this requirement include the velocity gradient tensor, the strain rate tensor, the vorticity tensor, the wall distance, and the scalar invariants derived from them (e.g., the magnitude of the strain rate, the magnitude of the vorticity, etc.). Following the covariance correction approach for transition models in reference [13], this paper reconstructs the $\gamma-\widetilde{\mathrm{Re}}_{\theta,t}$ transition model based on these Galilean invariants as follows:

(1) Normal-gradient formulation of the pressure gradient parameter

To eliminate the dependence on the streamwise coordinate, the pressure gradient parameter is expressed as a function of the velocity gradient in the wall-normal direction:

$$\lambda_{\theta L}=-7.57\times10^{-3}\frac{y^2}{\nu}\frac{\partial u}{\partial n_j}+0.0128 \tag{1}$$

where n_j is the unit vector normal to the wall, and $\frac{\partial u}{\partial n_j}$ denotes the velocity gradient component in the normal direction. This reconstruction is based on the continuity relation in boundary-layer theory: for incompressible flow, the streamwise velocity gradient and the normal velocity gradient are related through mass conservation.

(2) Galilean-invariant formulation of turbulence intensity

The conventional definition based on the free-stream velocity is replaced by a formulation based on the vorticity magnitude and the wall distance:

$$Tu_L=\min\left(100\frac{\sqrt{2k/3}}{\Omega y},100\right) \tag{2}$$

where Ω is the vorticity magnitude and y is the wall distance. This combination is dimensionally a

velocity, thereby ensuring the Galilean invariance of Tu_L.

(3) Reformulation of the momentum thickness Reynolds number transport equation

The convection term is replaced by a combination based on the strain rate magnitude, the vorticity magnitude, and the wall distance:

$$\rho\frac{\partial\widetilde{\mathrm{Re}_{\theta t}}}{\partial t}+\rho\frac{\partial}{\partial x_j}\left[\left(Sy\bullet t_j+\Omega y\bullet n_j\right)\widetilde{\mathrm{Re}_{\theta t}}\right]=P_{\theta t,L}+\frac{\partial}{\partial x_j}\left[D_{\theta t,L}\frac{\partial\widetilde{\mathrm{Re}_{\theta t}}}{\partial x_j}\right] \tag{3}$$

where t_j is the unit vector tangential to the wall, n_j is the unit vector normal to the wall. The combined quantities Sy and Ωy (or their specific forms) are dimensionally equivalent to velocities, representing shear-induced streamwise transport and rotation-induced normal transport, respectively, thereby ensuring the Galilean invariance of the convection term.

The source term is replaced by a formulation based on the combination of strain rate and vorticity:

$$P_{\theta t,L}=c_{\theta t}\rho(S+\alpha\Omega)\left(\mathrm{Re}_{\theta t}-\widetilde{\mathrm{Re}_{\theta t}}\right)\left(1-F_{\theta t}\right) \tag{4}$$

where $S+\alpha\Omega$ is a characteristic frequency combining strain and rotation effects, whose reciprocal is the time scale; α is a dimensionless weight coefficient, typically taken as $\alpha=2.0$. This combination has the dimensions of frequency, thus ensuring the Galilean invariance of the time scale in the source term.

The conventional isotropic diffusion coefficient is replaced by an anisotropic diffusion tensor based on the strain rate and vorticity tensors:

$$D_{\theta t,L}=\mu\delta_{ij}+\rho y^2\left[c_1S_{ij}+c_2\frac{S_{ik}\Omega_{kj}-\Omega_{ik}S_{kj}}{S+\varepsilon}\right]\bullet\left[1-e^{-\frac{\gamma}{\gamma_0}}\right] \tag{5}$$

In the above, the first term represents molecular viscous diffusion, and the second term is the turbulent diffusion constructed from the strain rate tensor and the vorticity tensor. The coefficients c_1 and c_2 control the degree of anisotropy and are generally set as $c_1=0.10, c_2=0.08$. This tensor has the dimensions of dynamic viscosity, and the function $1-e^{-\gamma/\gamma_0}$ is a modulation function for turbulent diffusion to avoid abrupt changes in the diffusion term across the transition region.

2.2 Crossflow Transition C1 Criterion Based on Local Variables

Under the Coriolis force due to rotation, the rotor exhibits significant spanwise flow, which readily triggers crossflow transition. To effectively predict crossflow instability, this paper introduces the crossflow C1 criterion. This criterion was proposed by Arnal et al.[14] from ONERA (the French Aerospace Lab) based on experimental data. It employs the crossflow displacement thickness Reynolds number $\mathrm{Re}_{\delta 2}$ as the key parameter for evaluating crossflow intensity, defined as follows:

$$\mathrm{Re}_{\delta 2}=\frac{\rho Q_e\delta_2}{\mu},\delta_2=\int_0^\infty\frac{|0-w|}{Q_e}dy \tag{6}$$

In the above formula, δ_2 is the crossflow displacement thickness of the boundary layer, Q_e is the freestream velocity at the edge of the three-dimensional boundary layer, and w is the crossflow velocity. The C1 criterion determines the occurrence of transition as follows: when the crossflow displacement thickness Reynolds number exceeds a certain critical value, crossflow transition is triggered. The expression for this critical value is:

$$\mathrm{Re}_{\delta 2t}=\begin{cases}\dfrac{300}{\pi}\tan^{-1}\left(\dfrac{0.106}{(H_{12}-2.3)^{2.05}}\right), & 2.3\le H_{12}\le 2.7\\ 150.0, & H_{12}<2.3\end{cases} \tag{7}$$

However, in the C1 criterion, variables such as the shape factor H_{12} and the displacement thickness δ_2 depend on integration along the boundary-layer normal direction, making them difficult to implement efficiently and reliably for complex configurations. Therefore, it is necessary to reformulate the crossflow intensity indicator into a form expressible in terms of local variables. Following the localization approach used for the transition momentum thickness Reynolds number in the $\gamma-\widetilde{\mathrm{Re}_{\theta,t}}$ transition model, a crossflow Reynolds number Re_w that does not require integration is constructed. It is defined as the ratio of the local turbulent crossflow shear stress to

the laminar crossflow shear stress, expressed as:

$$\mathrm{Re}_w = \frac{\tau_{turb,z}}{\tau_{lam,z}} = \frac{\rho y^2 (\frac{\partial w}{\partial y})^2}{\mu(\frac{\partial w}{\partial y})} = \frac{y^2}{\nu}\frac{\partial w}{\partial y} \tag{8}$$

To derive the relationship between the crossflow Reynolds number and the crossflow displacement thickness Reynolds number, it is necessary to utilize the similarity solution form of the crossflow Reynolds number expression, converting the dimensional wall distance and crossflow velocity into dimensionless form. The resulting dimensionless crossflow Reynolds number expression is:

$$\mathrm{Re}_w = \left(\frac{2x_w}{\nu(m+1)U_e}\right)^{\frac{1}{2}} \cdot Q_e \cos\phi \sin\phi \cdot Y^2 \left(G'(Y) - F''(Y)\right) \tag{9}$$

Following the same line of reasoning, the expression for the crossflow displacement thickness Reynolds number is obtained as follows:

$$\mathrm{Re}_{\delta 2} = \frac{Q_e}{\nu}\delta_2 = \left(\frac{2x_w}{\nu(m+1)U_e}\right)^{\frac{1}{2}} \cdot Q_e \cos\phi \sin\phi \cdot \int_0^\infty \left|G(Y) - F'(Y)\right| dY \tag{10}$$

Finally, the ratio between them is obtained as:

$$r = \frac{\mathrm{Re}_w}{\mathrm{Re}_{\delta 2}} = \frac{Y^2\left(G'(Y) - F''(Y)\right)}{\int_0^\infty \left|G(Y) - F'(Y)\right| dY} \tag{11}$$

This ratio depends only on the Hartree parameter β, the local sweep angle ϕ, and the dimensionless wall-normal distance Y. For given β and ϕ, the maximum value of this ratio at a certain location within the boundary layer can be obtained by searching along the Y direction.

Traditional non-local variables such as the shape factor are generally obtained by solving the Falkner–Skan–Cooke similarity equations. To improve the computational efficiency of transition prediction and avoid repeatedly solving the Falkner–Skan–Cooke equations during the solution process, this paper adopts an offline database approach. Using the Hartree parameter $\beta \in [-0.198, 2.4]$ (step 0.001) and the sweep angle $\phi \in [0°, 180°]$ (step 1°) as indices, the similarity equations are solved in advance to construct the mapping relationships with the shape factor, the pressure gradient parameter, and the peak value of the ratio $r_{\max}$, thereby establishing a database. In actual CFD calculations, the corresponding H_{12} and the peak ratio $r_{\max}$ at a given point are obtained by querying the database, from which the critical crossflow displacement thickness Reynolds number and the equivalent $\mathrm{Re}_{\delta 2}$ are derived. Finally, the localized crossflow transition criterion is obtained as follows:

$$F_{onset1,C1} = \frac{\mathrm{Re}_w}{r_{\max}\,\mathrm{Re}_{\delta 2t}} \tag{12}$$

2.3 Construction of the $G-\gamma-\widetilde{\mathrm{Re}}_{\theta,t}-C1$ Transition Model

This section describes the construction approach of the proposed $G-\gamma-\widetilde{\mathrm{Re}}_{\theta,t}-C1$ transition model as follows:

(1) Using the covariance-corrected model as the foundation: The transport equation framework reconstructed in Section 2.1 is adopted, i.e., the pressure gradient parameter, turbulence intensity, convection term and source term of the momentum thickness Reynolds number are all expressed in terms of Galilean invariants such as strain rate, vorticity, and wall distance. This foundation ensures the consistency of model predictions under any moving coordinate system and eliminates the non-physical transition deviations caused by reference frame changes in rotor numerical simulations.

(2) Embedding the localized crossflow transition criterion: The transition criterion is extended from two dimensions to three dimensions and integrated into the source term of the intermittency factor transport equation. The modified source term of the intermittency factor transport equation is as follows:

$$P_\gamma = F_{length_3D} c_{a1} \rho S \left[\gamma F_{onset_3D} \right]^{0.5} (1 - c_{e1}\gamma) \tag{13}$$

where the transition onset factor F_{onset_3D} is defined as follows:

$$\begin{cases} F_{onset1_TS} = \dfrac{\mathrm{Re}_v}{2.193\,\mathrm{Re}_{\theta c}}, \quad F_{onset1_C1} = \dfrac{\mathrm{Re}_w}{f(\lambda_\theta, \phi)\,\mathrm{Re}_{\delta 2t}} \\ F_{onset1_3D} = \max(F_{onset1_TS}, F_{onset1_C1}) \\ F_{onset2_3D} = \min(\max(F_{onset1_3D}, F^4_{onset1_3D}), 2.0) \\ F_{onset3_3D} = \max(1 - (\dfrac{RT}{2.5})^3, 0.0) \\ F_{onset_3D} = \max(F_{onset2_3D} - F_{onset3_3D}, 0.0) \end{cases} \tag{14}$$

The transition region length factor under the C1 criterion for crossflow transition is defined as:

$$F_{length_C1} = \begin{cases} \left[\begin{array}{l} 398.189 \cdot 10^{-1} - (993.917 \cdot 10^{-5}) \widetilde{\mathrm{Re}_{CF}} \\ -(920.604 \cdot 10^{-7}) \widetilde{\mathrm{Re}_{CF}}^2 \end{array} \right], & \widetilde{\mathrm{Re}_{CF}} < 480 \\ \left[\begin{array}{l} 263.404 - (103.283 \cdot 10^{-2}) \widetilde{\mathrm{Re}_{CF}} + \\ (135.103 \cdot 10^{-5}) \widetilde{\mathrm{Re}_{CF}}^2 - (588.513 \cdot 10^{-9}) \widetilde{\mathrm{Re}_{CF}}^3 \end{array} \right], & 480 \le \widetilde{\mathrm{Re}_{CF}} < 715.2 \\ \left[0.5 - (\widetilde{\mathrm{Re}_{CF}} - 715.2) \cdot 2.5 \cdot 10^{-4} \right], & 715.2 \le \widetilde{\mathrm{Re}_{CF}} < 1440 \\ [0.3188], & 1440 \le \widetilde{\mathrm{Re}_{CF}} \end{cases} \tag{15}$$

In the formula, $\widetilde{Re}_{CF} = \widetilde{Re}_{\theta,t} \bullet \cos\phi$ represents the effective Reynolds number in the crossflow direction. During the simulation, if the transition is dominated by crossflow instability, the crossflow transition region length factor is selected; if it is dominated by streamwise instability, the streamwise transition region length factor from the original model is used. Combining both, the three-dimensional transition region length factor is obtained as:

$$F_{length_3D} = \begin{cases} F_{length_TS}, & (F_{onset1_TS} \ge F_{onset1_C1}) \\ F_{length_C1}, & (F_{onset1_TS} < F_{onset1_C1}) \end{cases} \tag{16}$$

By incorporating the crossflow transition criterion through the transition onset factor and the transition region length factor, the transition model is extended to three dimensions in terms of the intermittency factor and the generation mechanism of turbulent kinetic energy, enabling it to capture transition processes triggered by both streamwise and crossflow instabilities.

(3) Strictly maintaining the local-variable nature of the model: To avoid introducing non-local operations that would undermine the efficiency and robustness of the original model, all parameters used to judge crossflow transition—including the local crossflow Reynolds number, the pressure gradient factor, and the sweep angle—are obtained based on local flow-field variables through algebraic relations or database queries. This approach requires no integration along the boundary-layer normal or identification of the boundary-layer edge, thereby ensuring the model's applicability to complex rotor configurations and large-scale parallel computations.

2.4 Coupling of the Transition Prediction Model with the Solver

PMNS3DR is a three-dimensional flow numerical simulation program developed by our research group, capable of computing the aerodynamic characteristics of three-dimensional geometries and performing detailed flow field analysis. The program can solve both steady and unsteady Euler/RANS equations, and integrates turbulence models such as the Baldwin–Lomax (BL) model, the Spalart–Allmaras model, and the SST two-equation model. For spatial discretization, it provides various schemes including the central scheme, Roe scheme, AUSM-family schemes, and the WENO scheme. For time advancement, it includes explicit Runge–Kutta schemes, implicit LU-SGS schemes, and other methods. In addition, the program incorporates convergence acceleration techniques such as local time stepping, residual smoothing, and multigrid methods, enabling efficient and accurate unsteady computations of rotors and propellers.

Coupling strategy between the transition model and the solver: The transition model outputs an effective intermittency factor, which is used to modulate the production term of the turbulent kinetic energy equation in the SST model, thereby controlling the generation and development of turbulence. Meanwhile, the flow-field information provided by the turbulence model also lays the foundation for the transition model to compute key parameters such as the local turbulence

intensity. Thus, the flow solver, the turbulence model, and the transition model form a tightly coupled closed-loop computational system. In this paper, the unsteady RANS solver integrated with the automatic transition prediction capability is named PMNS3DR-T, and its coupling computation procedure is shown in Figure 1:

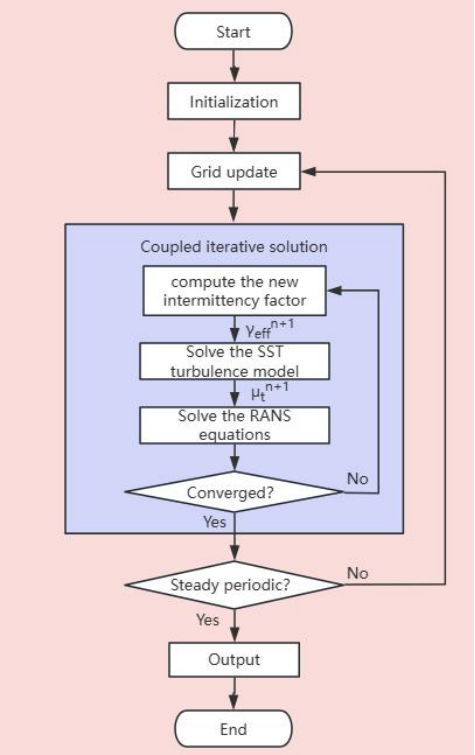


Figure 1 Schematic diagram of the coupling computation procedure

(1) Initialization:

Set the far-field boundary conditions, free-stream turbulence intensity, and viscosity ratio, and initialize the flow-field variables.

(2) Time-step loop:

1. Mesh update: Update the blade mesh position according to the rotor motion, and complete the hole-cutting mapping and interpolation reconstruction for the overset grid.
2. Coupled iterative solution (sub-iteration loop):

- Step 1: Based on the current flow-field information (velocity, density, etc.), k^n and ω^n, compute the new γ_{eff}^{n+1} using the transition model.
- Step 2: Use the computed γ_{eff}^{n+1} to modulate the production term of the turbulent kinetic energy in the SST model, and solve for the updated k^{n+1}, ω^{n+1}, and eddy viscosity μ_t^{n+1}.
- Step 3: With the newly computed μ_t^{n+1}, solve the RANS equations to obtain the updated flow-field information.
- Step 4: Check whether the residuals satisfy the sub-iteration convergence criterion. If converged, complete the current physical time step; otherwise, continue iterating.

(3) Output:

After the flow field reaches a statistically steady periodic condition, output the flow-field information, aerodynamic coefficients, and transition location.

2.5 Validation Case

The 6:1 ellipsoid case[16] is used to validate the improved model. The test model has a chord length of 2.4 m, a free-stream turbulence intensity of 0.2%, and a wind speed of 45 m/s. To verify the crossflow transition prediction capability of the improved model, a 30° angle-of-attack condition dominated by crossflow transition is selected for numerical simulation validation. The computed conditions are as follows: $Ma = 0.136$, $Re = 7.2 \times 10^6$, $Tu = 0.5\%$, $RT = 5$.

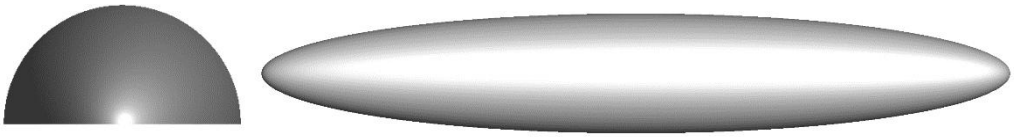
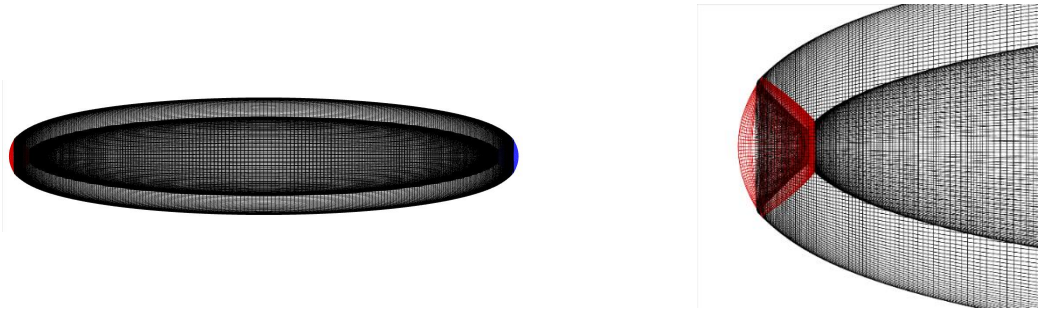


Figure 2 Schematic of the 6:1 ellipsoid geometry

A schematic of the body-fitted grid is shown in Figure 3. The body-fitted grid consists of 4,582,000 cells, with a first-layer cell height of 2×10^{-6} to ensure $y^+<1$. The background grid is a Cartesian grid with a far-field distance of 20 times the chord length, resulting in a total cell count of 20,366,136. The hole-cutting relationship between the body-fitted grid and the background grid is illustrated in Figure 4.



(a)Overall schematic diagram **(b)Local detailed view of the overset grid**

Figure 3 Schematic of the ellipsoid body- fitted grid

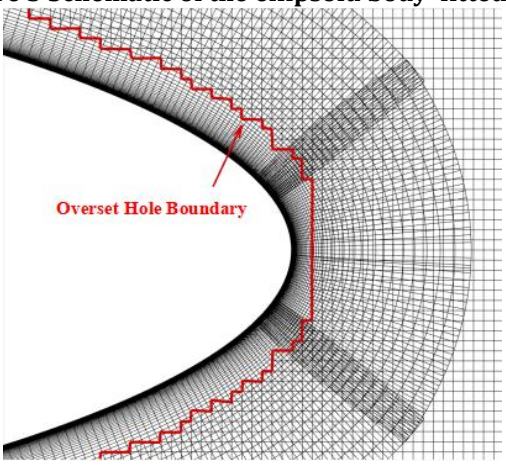


Figure 4 Schematic of the hole boundary for the overset grid

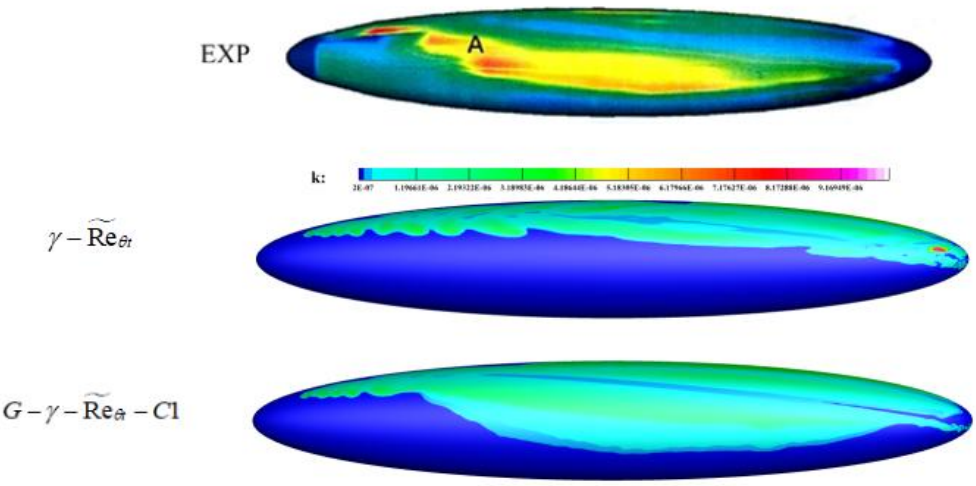


Figure 5 Comparison of transition locations among different transition models

Figure 5 shows a comparison of transition locations predicted by different transition models. From the results, it can be observed that the $\gamma-\widetilde{\mathrm{Re}}_{\theta,t}$ model without the crossflow transition criterion predicts a significantly larger laminar region and fails to accurately capture the change in transition location caused by crossflow instability beyond the 25% chord length station of the ellipsoid. In contrast, the transition model coupled with the C1 criterion successfully captures this trend and

accurately reflects the influence of crossflow on the transition process.

3. Prediction Results and Analysis of Rotor Transition Characteristics

3.1 Introduction to the PSP Rotor Transition Measurement Experiment

To evaluate the predictive capability of the developed transition model for the transition phenomenon in rotor flows, this study selects the widely used PSP rotor benchmark case for comparative validation. The data for this case originate from a series of experiments conducted by Overmeyer, Martin, et al.[17] in 2016 at the Rotor Test Facility of NASA Langley Research Center. Its prominent advantage lies in providing a publicly available test model with clearly defined geometry, as well as high-precision transition location data obtained through advanced measurement techniques, thereby offering a reliable basis for the validation of numerical models.

The planform geometry of the rotor is shown in Figure 6. The rotor blade has a radius of 1.6891 m and a chord length of 0.1384 m. The blade section employs a combination of three airfoil types (RC(4)-12, RC(4)-10, and RC(6)-08) and features a linear twist of −14°.

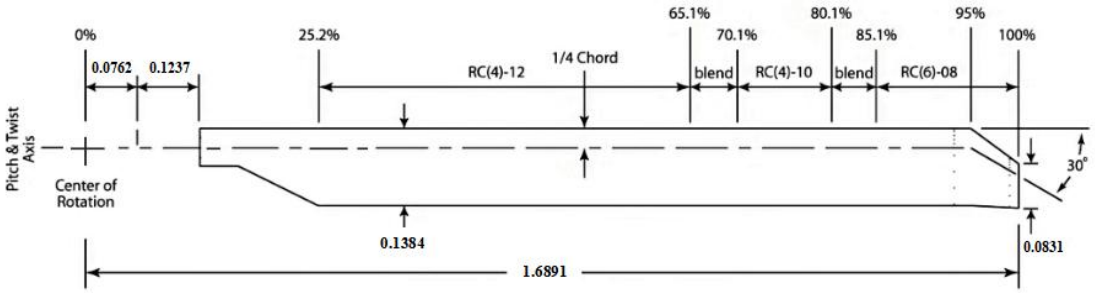


Figure 6 Schematic diagram of the PSP rotor planform geometry[17]

For capturing the transition location, the experiment employed differential infrared thermography. This method achieves non-contact, full-field, and accurate identification of the transition boundary by resolving the subtle temperature variations on the blade surface caused by differences in frictional heating between laminar and turbulent regions. The transition location was obtained by averaging 575 instantaneous infrared images, effectively reducing random errors and ensuring the stability and reliability of the data. Figure 7 shows the measured temperature distribution and a schematic of the extracted transition location.

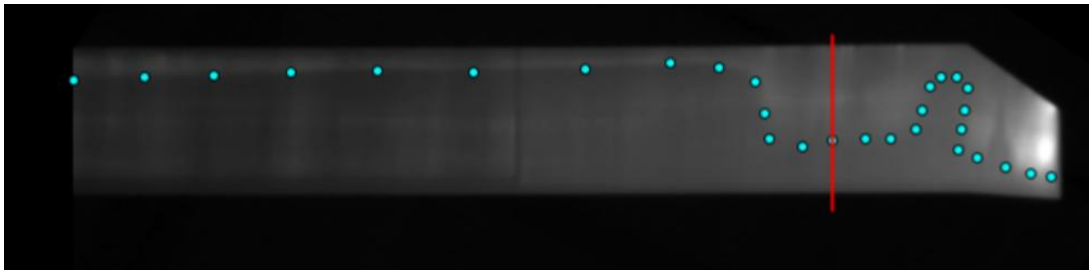


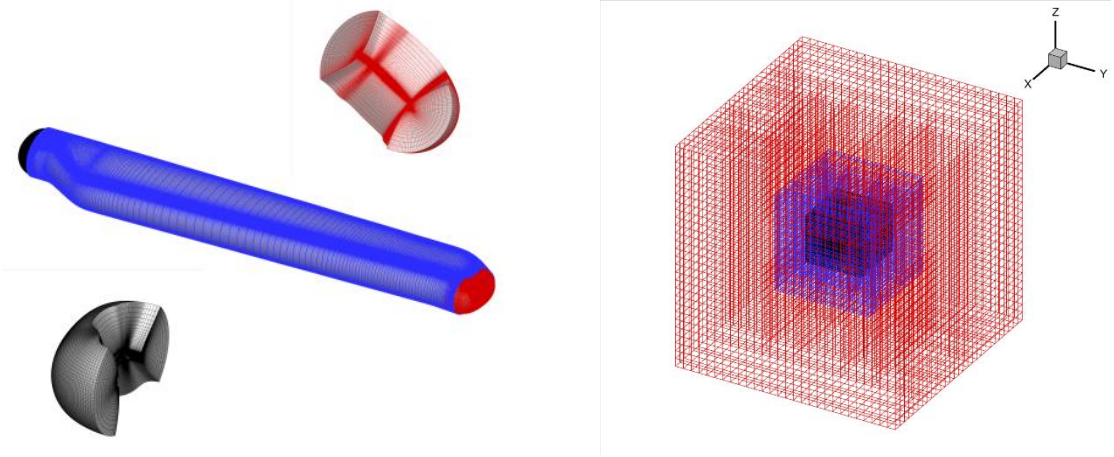
Figure 7 Schematic of the PSP rotor infrared thermography image[17]

3.2 Prediction of Hover Transition and Model Comparative Analysis

For the hovering condition, the rotor under consideration is a four-bladed rotor with a solidity of 0.1033, a tip Mach number of 0.58, and a tip Reynolds number of 1.7×10^6 based on the reference chord length. To systematically investigate the rotor transition characteristics under different operating loads, three typical thrust coefficient conditions CT/σ=0.050, 0.064 and 0.085 are selected for numerical simulation, corresponding to pitch angles of 6°, 8°, and 10°, respectively. These conditions broadly cover typical hover scenarios from moderate to relatively high loads, offering good representativeness and analytical value.

A schematic of the computational grid is shown in Figure 8. To ensure accurate resolution of the near-wall flow, the first-layer grid height on each blade surface is set to 2×10^{-6}, satisfying the requirement of $y+<1$. The grid expansion ratio is 1.08 to guarantee precise resolution of the boundary-layer flow. To further capture flow details in critical regions, local refinement is applied to the leading and trailing edges, the tip region, the swept transition region, and the airfoil transition regions, ensuring sufficient spatial resolution in areas with strong geometric features or high flow gradients. After the above treatment, the total number of grid cells on a single blade surface reaches 5,298,688. The far-field boundary of the background grid is set at a distance of 20 rotor diameters from the rotation center, aiming to reduce potential interference of far-field boundary conditions on the near-field complex flow while ensuring that the free-stream turbulence intensity does not decay excessively before reaching the blade surface, thereby providing a more realistic

simulation of the actual turbulent environment.



(a) Blade body- fitted grid **(b) Overall computational grid**

Figure 8 Schematic of the PSP rotor computational grid

Figure 9 shows a comparison of the rotor hover efficiency predicted by the original $\gamma-\widetilde{\mathrm{Re}}_{\theta,t}$ model and the improved transition model proposed in this paper against experimental data. The experimental data include two cases: free transition and fixed transition at 5% chord length on both the upper and lower surfaces, which represent the theoretical upper and lower limits of the actual hover efficiency, respectively, thus providing a complete confidence interval for model evaluation.

From the comparison results, it can be seen that the hover efficiency predicted by the original $\gamma-\widetilde{\mathrm{Re}}_{\theta,t}$ model is slightly higher than the free transition experimental value, exceeding the upper bound of the confidence interval. In contrast, the prediction results of the $G-\gamma-\widetilde{\mathrm{Re}}_{\theta,t}-C1$ model developed in this paper lie between the free transition and fixed transition experimental values, are close to the free transition experimental value, and show better agreement with the experimental data.

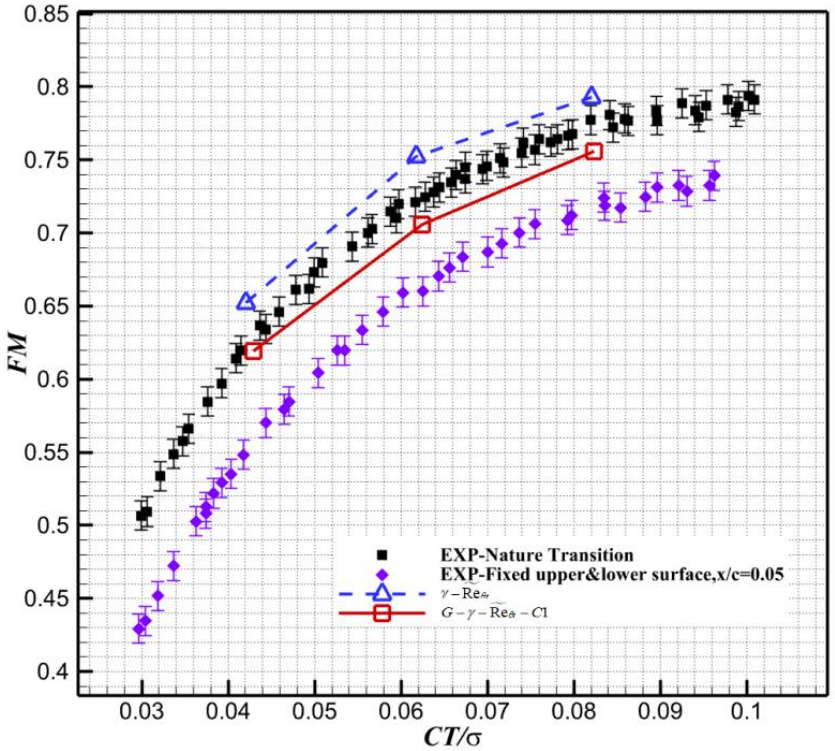


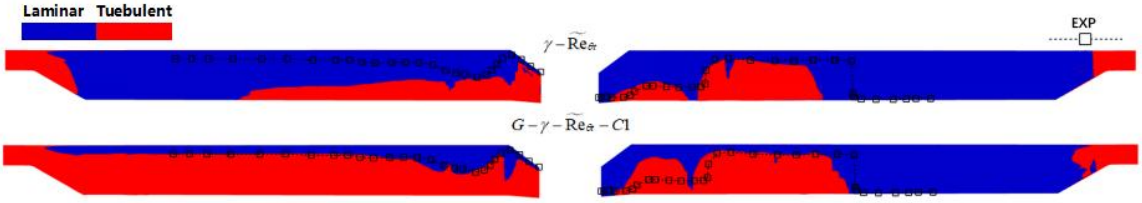
Figure 9 Comparison of computed hover efficiency with experimental data

Figure 10 Figure 12 present the numerical simulation predictions of the laminar flow regions and transition locations on the blade surface under three typical thrust coefficient conditions of 0.050, 0.064, and 0.085, respectively. In the contour plots, blue and red regions denote laminar and turbulent flow states, respectively.

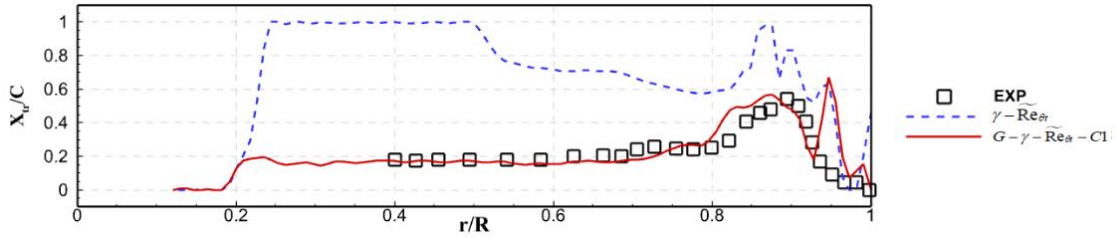
Regarding the overall trend of transition location variation with pitch angle, the numerical simulation results show good agreement with the wind tunnel experimental data: as the pitch angle increases, the transition point on the upper surface gradually moves forward toward the leading edge, while

the transition point on the lower surface continuously shifts downstream toward the trailing edge. This variation is mainly attributed to the change in effective angle of attack caused by the increased pitch angle, which in turn affects the pressure distribution and boundary-layer velocity profile on the blade surface. It is worth noting that, comparing the sensitivity of the transition point to pitch angle changes between the upper and lower surfaces, the transition location on the lower surface exhibits significantly higher sensitivity to pitch angle variations than that on the upper surface. This indicates that in the lower surface flow, factors such as pressure gradient and external disturbances have a more pronounced influence on boundary-layer stability, leading to a higher sensitivity of its transition characteristics to changes in pitch angle.

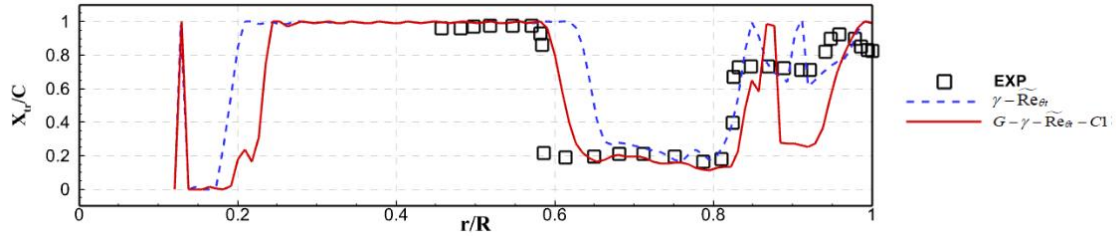
For the thrust coefficient condition of 0.050 ($\theta = 6°$), the comparison between the predictions of each transition model and the experimental values is as follows: The $\gamma - \widetilde{\mathrm{Re}}_{\theta,t}$ model predicts a noticeably larger laminar region on the upper surface. On the lower surface, although the overall agreement is reasonable, the predicted laminar region remains too large in the radial range of r/R=60%–70%. Moreover, due to its lack of covariance, the $\gamma - \widetilde{\mathrm{Re}}_{\theta,t}$ model exhibits unphysical oscillations in some regions, particularly near the blade tip. In contrast, the $G-\gamma-\widetilde{\mathrm{Re}}_{\theta,t}-C1$ model based on Galilean invariance effectively eliminates these oscillations, yielding a smoother predicted transition curve. Furthermore, by accounting for crossflow transition effects, the $G-\gamma-\widetilde{\mathrm{Re}}_{\theta,t}-C1$ model predicts an upper-surface transition location that is essentially consistent with the experimental data, except that the predicted laminar region is somewhat too large near the swept transition location at the blade tip (r/R=0.95). On the lower surface, however, because the crossflow transition criterion in this model does not fully account for the spanwise variation of rotational effects, the predictions agree well with experiments in the mid-span region but underpredict the extent of the laminar region.



(a) Schematic of the blade surface laminar flow extent



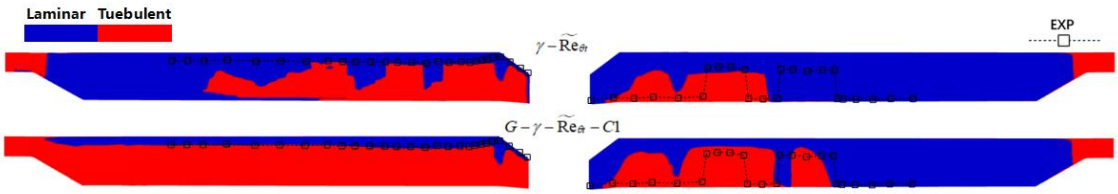
(b) Upper-surface transition location comparison



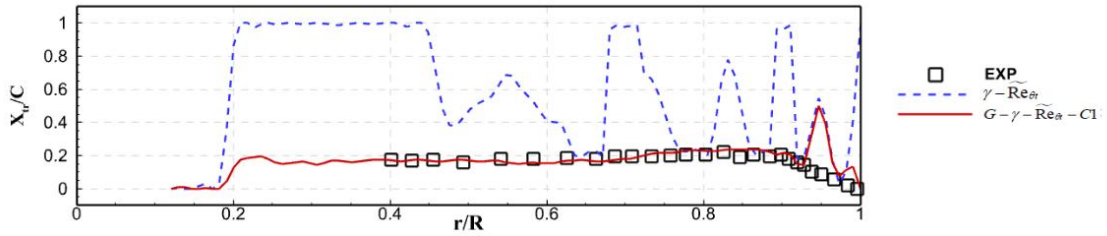
(c) Lower-surface transition location comparison

Figure 10 Comparison of computed transition location with experimental data at CT /σ=0.050

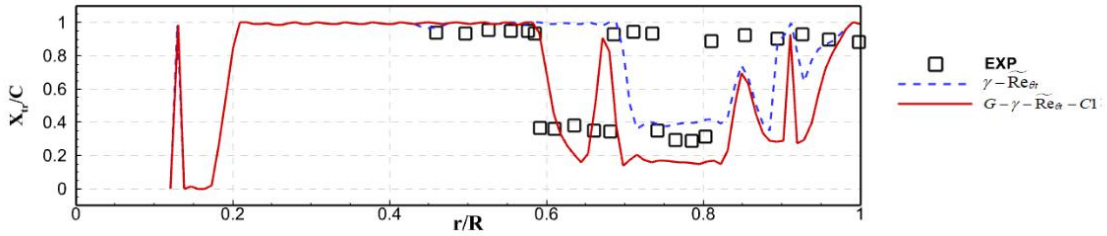
For the thrust coefficient condition of 0.064 ($\theta = 8°$): The $\gamma - \widetilde{\mathrm{Re}}_{\theta,t}$ model predicts an excessively large laminar region and fails to capture the trend of the laminar region variation on the lower surface within the radial range of r/R=60%–80%. In contrast, the $G-\gamma-\widetilde{\mathrm{Re}}_{\theta,t}-C1$ model shows good agreement with the experimental data on both the upper and lower surfaces. Specifically, the transition location predicted by this model on the upper surface is highly consistent with the experimental results except for a noticeable rearward shift near r/R=95%; on the lower surface, although the predicted laminar region is slightly smaller than the experimental value, the overall trend is essentially consistent.



(a) Schematic of the blade surface laminar flow extent



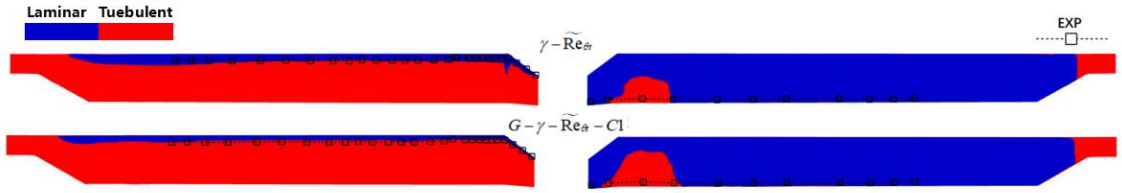
(b) Upper-surface transition location comparison



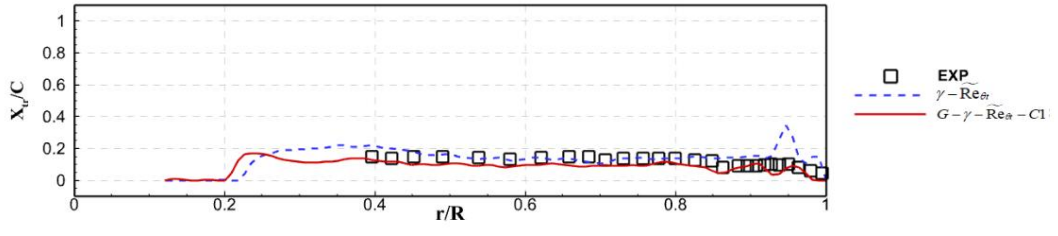
(c) Lower-surface transition location comparison

Figure 11 Comparison of computed transition location with experimental data at CT /σ=0.064

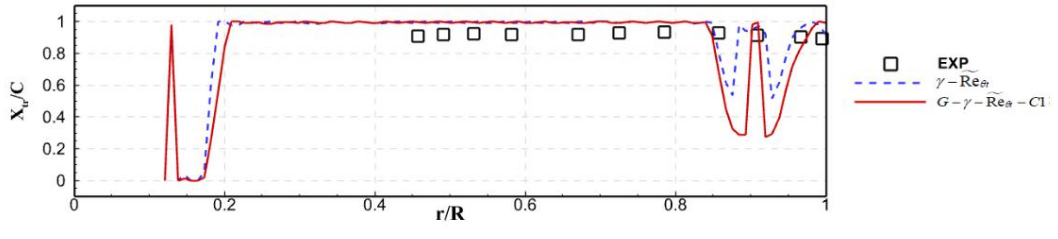
For the thrust coefficient condition of 0.085 ($\theta=10°$): Due to the excessively large pitch angle, the experimental data exhibit nearly fully turbulent flow on the upper surface and nearly fully laminar flow on the lower surface. The predictions of the two transition models are essentially consistent with each other and agree well with the experimental data overall, except that in the radial range of r/R=85%–95% on the lower surface, the computed transition location is closer to the leading edge than the experimental value. Among them, the $G-\gamma-\widetilde{Re}_{\theta,t}-C1$ model predicts a slightly more forward transition location because it accounts for crossflow transition effects.



(a) Schematic of the blade surface laminar flow extent



(b) Upper-surface transition location comparison



(c) Lower-surface transition location comparison

Figure 12 Comparison of computed transition location with experimental data at CT /σ=0.085

Overall, for the numerical simulation of rotor hover transition characteristics, the

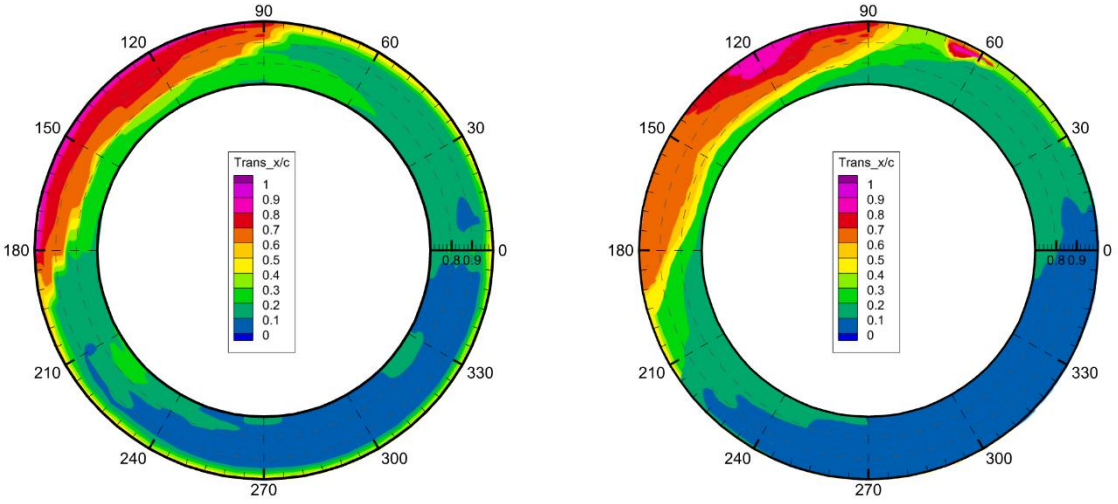
$G-\gamma-\widetilde{\mathrm{Re}}_{\theta,t}-C1$ model developed in this paper more accurately predicts the spanwise variation of the transition location on both the upper and lower surfaces of the rotor. The predicted transition locations are in good agreement with the experimental data. Moreover, by introducing the covariance correction, the model effectively eliminates the non-physical errors of the $\gamma-\widetilde{\mathrm{Re}}_{\theta,t}$ model caused by its inadequate prediction of rotational motion, thereby enabling a more accurate evaluation of the rotor blade transition characteristics under hovering conditions.

3.3 Prediction of Forward-Flight Transition and Model Comparative Analysis

For the forward-flight case, the rotor under consideration is a three-bladed rotor with a solidity of 0.077, a tip Mach number of 0.55, a tip Reynolds number of 1.6×10^6 based on the reference chord length, an advance ratio of 0.3, and a pitch angle motion law given by: $\theta(t)=9.71^\circ+3.58^\circ\cos\psi(t)-7.37^\circ\sin\psi(t)$.

The blade grid employed is the same as that used for the hovering case. The background grid extends to a distance of 25 rotor diameters in the streamwise direction (the positive x-axis direction) behind the rotor to cover the fully developed wake region during forward flight.

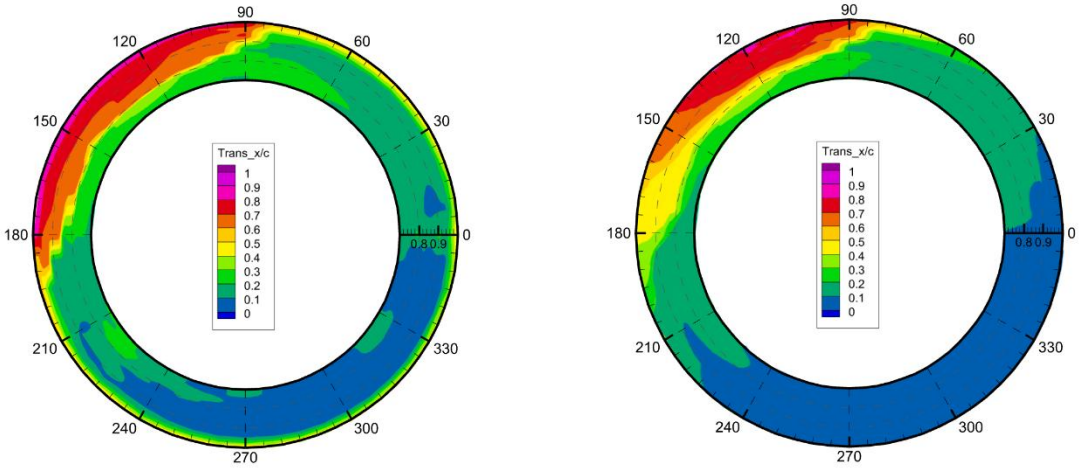
Figure 13 and Figure 14 present the comparison of the upper-surface transition locations predicted by the two transition models with the experimental data in the radial range of r/R=70%–100% during the last revolution. The experimental data show the following variation of transition location with azimuthal angle: within the azimuthal range of 0° to 120° (corresponding to most of the advancing side of the rotor), the transition location gradually moves downstream, reaching a maximum near 120° at approximately 70% to 90% of the chord length. Thereafter, the transition location begins to move upstream, and when the azimuthal angle approaches 180° (transitioning from the advancing side to the retreating side), the transition location undergoes a drastic change, dropping to within 20% of the chord length. On the retreating side, the transition location remains below 20% of the chord length, with most of the region being fully turbulent. Only in a limited region near the blade tip do the experimental data indicate that transition still occurs, approximately at 10% of the chord length.



(a) Experimental transition location **(b) $\gamma-\widetilde{\mathrm{Re}}_{\theta,t}$ Model transition location**

Figure 13 Comparison of predicted and experimental transition locations ($\gamma-\widetilde{\mathrm{Re}}_{\theta,t}$ model)

The transition location predicted by the $\gamma-\widetilde{\mathrm{Re}}_{\theta,t}$ model generally follows the trend of the experimental data with azimuthal angle, but the following discrepancies remain: In most regions, the predicted transition location is slightly smaller than the experimental value. Near the blade tip on the retreating side, the model fails to effectively capture the transition location. In the vicinity of 120° azimuth, the maximum transition location predicted by the model is further downstream compared to the experimental value. Additionally, near the blade tip at an azimuth of approximately 60°, the model anomalously predicts an excessively large laminar region.



(a) Experimental transition location **(b) $G-\gamma-\widetilde{\mathrm{Re}}_{\theta,t}-C1$ Model transition location**

Figure 14 Comparison of predicted and experimental transition locations ($G-\gamma-\widetilde{\mathrm{Re}}_{\theta,t}-C1$ model)

The $G-\gamma-\widetilde{\mathrm{Re}}_{\theta,t}-C1$ model effectively eliminates the anomalous behavior of the $\gamma-\widetilde{\mathrm{Re}}_{\theta,t}$ model near the 60° azimuth. Moreover, by further accounting for the influence of crossflow transition, the predicted variation trend of transition location with azimuthal angle agrees better with the experimental data. A shortcoming is that the predicted transition location is slightly ahead of the experimental value.

In addition, it should be noted that the numerical simulations in this paper do not include the Robin Mod-7 fuselage beneath the rotor. According to the study by Jain[18], the presence of the fuselage has a certain impact on transition prediction and leads to differences in transition distribution at different azimuthal angles. Therefore, in future work, the fuselage configuration will be incorporated into the numerical simulations to further improve the accuracy of transition prediction.

4. Conclusion

This paper investigates numerical simulation methods for boundary-layer transition characteristics applicable to rotors, driven by the demand for refined rotor numerical simulation and natural laminar flow rotor design. To address the shortcomings of the traditional $\gamma-\widetilde{\mathrm{Re}}_{\theta,t}$ transition model, namely its lack of covariance under moving reference frames and its inability to predict crossflow transition, corresponding improvements are made. The main work and conclusions are as follows:

(1) Covariance correction based on Galilean invariants is achieved. The pressure gradient parameter, the turbulence intensity parameter, and the key terms in the momentum thickness Reynolds number transport equation in the $\gamma-\widetilde{\mathrm{Re}}_{\theta,t}$ model are replaced by Galilean invariants such as strain rate and vorticity. The improved model exhibits good predictive consistency under different moving coordinate systems, laying the foundation for predicting transition characteristics of rotors under rotational motion.

(2) The model's capability to capture crossflow transition is extended using the C1 criterion, leading to the development of the $G-\gamma-\widetilde{\mathrm{Re}}_{\theta,t}-C1$ model. By deriving the relationship between the crossflow Reynolds number and the crossflow displacement thickness Reynolds number, and constructing a parameter database for local variables and transition variables, the C1 criterion is implemented in a localized manner. The model coupling is achieved by modifying the intermittency factor transport equation. The improved model can reasonably reflect the influence of crossflow instability on transition.

(3) The developed transition prediction model is coupled with an unsteady RANS solver to obtain a high-fidelity unsteady RANS solver capable of automatically predicting rotor transition. Based on the experimental data of the PSP rotor, the predictive capabilities of the improved model and the original model for transition characteristics are systematically compared. The results show that the $G-\gamma-\widetilde{\mathrm{Re}}_{\theta,t}-C1$ transition model and the unsteady RANS solver with automatic transition prediction developed in this paper can accurately predict the transition location and aerodynamic performance of the rotor, providing a refined analysis tool for high-fidelity numerical simulation and laminar flow design of rotors.

Future work will include the following aspects to further improve the prediction accuracy of rotor transition characteristics and aerodynamic performance:

(1) Investigate transition characteristics under rotor-uselage interaction. This paper mainly focuses on an isolated rotor. In future work, a full configuration including the fuselage will be established to study the influence of the fuselage on the rotor flow field and transition process.
(2) Improve model parameter calibration and validation. The current model still exhibits deviations in local regions such as the blade tip. Further systematic calibration and optimization of key model parameters will be carried out using more wind tunnel experimental data.

5. Acknowledgment

This work was supported by the National Key Research and Development Program of China under Grant (No. 2023YFB3002800). The work was carried out at the National Supercomputer Center in Xi'an, and the calculations were performed on Sugon.

6. Contact Author Email Address

xujh@nwpu.edu.cn

7. Copyright Statement

The authors confirm that they, and/or their company or organization, hold copyright on all of the original material included in this paper. The authors also confirm that they have obtained permission from the copyright holder of any third party material included in this paper, to publish it as part of their paper. The authors confirm that they give permission, or have obtained permission from the copyright holder of this paper, for the publication and distribution of this paper as part of the ICAS proceedings or as individual offprints from the proceedings.

References

[1] Gardner A D, Wolf C C, Heineck J, et al. Helicopter Rotor Boundary Layer Transition Measurement in Forward Flight Using an Infrared Camera[C]. 75th Annual Forum & Technology Display of the Vertical Flight Society. Philadelphia, PA: VFS, 2019: 2-14.
[2] Gardner A D, Weiss A, Heineck J T, et al. Boundary Layer Transition Measured by DIT on the PSP Rotor in Forward Flight[J]. Journal of the American Helicopter Society, 2021, 66(2): 1-10.
[3] AIAA Rotorcraft Hover Prediction Workshop. 10 Years of AIAA Hover Prediction Workshops: State of the Art and Future Plans. https://www.aiaa-hpw.org/hpw-vision.
[4] Sheng C, Zhao Q, Hill M. Computational Investigation of a Full-Scale Proprotor Hover Performance and Flow Transition[J]. Journal of aircraft, 2018, 55(1): 122-132.
[5] Min B Y, Reimann C A, Wake B, et al. Hovering Rotor Simulation using OVERFLOW with Improved Turbulence Model[C]. 56th AIAA aerospace sciences meeting 2018: 1779.
[6] Carnes J, Coder J G. Computational Assessment of the HVAB Rotor in Hover Using Laminar-Turbulent Transition Modeling[C]. Applied aerodynamics, AIAA SciTech forum and exposition. 2019: 0288.
[7] Singh R, Corle E, Jain R, et al. Computation and Quantification of Uncertainty in Predictions of HVAB Rotor Performance in Hover[C]. AIAA Scitech 2019 Forum. San Diego, CA: AIAA, 2019: 0285.
[8] Zhao M, Xiao Z X, Fu S. Predictions of Transition on a Hovering Tilt-Rotor Blade[J]. Journal of Aircraft, 2014, 51(6): 1904-1913.
[9] Lee B, Govindarajan B, Baeder J. Methods for Efficient Resolution of Vortical Structures of an S-76 Rotor in Hover[C]. 55th AIAA Aerospace Sciences Meeting. Grapevine, 2017: 1664.
[10] Jain R. CFD Performance and Turbulence Transition Predictions on an Installed Model-scale Rotor in Hover[C]. 55th AIAA Aerospace Sciences Meeting. Grapevine, 2017: 1871.
[11] Park S, Kwon O J. Numerical Study of Isolated and Full Configuration PSP Rotor Using a Mixed Mesh Flow Solver[C]. AIAA Scitech 2020 Forum. Orlando, 2020: 0529.
[12] F. R. Menter, R. B. Langtry, S. R. Likki, et al. A Correlation-Based Transition Model Using Local Variables—Part I: Model Formulation[J]. Journal of Turbomachinery, 2006, 128(3): 57-67.
[13] Venkatachari B S, Paredes P, Derlaga J M, et al. Assessment of Transition Modeling Capability in OVERFLOW with Emphasis on Swept-Wing Configurations[C]. AIAA Scitech 2020 Forum. Orlando, 2020: 1034.
[14] Arnal D, Houdeville R, Séraudie A, et al. Overview of laminar-turbulent transition investigations at ONERA Toulouse[C]. 41st AIAA Fluid Dynamics Conference and Exhibit. 2011: 3074.
[15] DM Somers. Design and experimental results for the S809 airfoil [R] . NREL/SR-440-6918.
[16] Kreplin H P, Vollmers H, Meier H U. Wall Shear Stress Measurements on an Inclined Prolate Spheroid in the DFVLR 3M×3M Low Speed Wind Tunnel, Göttingen[J]. DFVLR-AVA, Report IB, 1985: 22-84.

[17] Overmeyer A D, Martin P B. Measured Boundary Layer Transition and Rotor Hover Performance at Model Scale[C]. 55th AIAA Aerospace Sciences Meeting. Grapevine, 2017: 1872.

[18] Jain R. CFD Performance and Turbulence Transition Predictions on an Installed Model-scale Rotor in Hover[C]. 55th AIAA Aerospace Sciences Meeting, January, 2017: 18.